Probing Star Formation in Galaxies at $z \approx 1$ via a Giant Metrewave Radio Telescope Stacking Analysis

Apurba Bera[1], Nissim Kanekar[1,4] , Benjamin J. Weiner[2] , Shiv Sethi[3], and K. S. Dwarakanath[3]
[1] National Center for Radio Astrophysics, Tata Institute of Fundamental Research, Pune University, Pune-411007, India; nkanekar@ncra.tifr.res.in
[2] Steward Observatory, Department of Astronomy, University of Arizona, Tucson, AZ 85721, USA
[3] Department of Astronomy and Astrophysics, Raman Research Institute, C.V Raman Avenue, Bengaluru, India

Abstract

We report deep Giant Metrewave Radio Telescope (GMRT) 610 MHz continuum imaging of four subfields of the DEEP2 Galaxy Redshift Survey. We stacked the radio emission in the GMRT images from a near-complete (absolute blue magnitude $M_B \leqslant -21$) sample of 3698 blue star-forming galaxies with redshifts $0.7 \lesssim z \lesssim 1.45$ to detect (at $\approx 17\sigma$ significance) the median rest-frame 1.4 GHz radio continuum emission of the sample galaxies. The stacked emission is unresolved, with a rest-frame 1.4 GHz luminosity of $L_{1.4GHz} = (4.13 \pm 0.24) \times 10^{22}$ W Hz^{-1}. We used the local relation between total star formation rate (SFR) and 1.4 GHz luminosity to infer a median total SFR of $(24.4 \pm 1.4)\, M_\odot$ yr^{-1} for blue star-forming galaxies with $M_B \leqslant -21$ at $0.7 \lesssim z \lesssim 1.45$. We detect the main-sequence relation between SFR and stellar mass, $M_\star$, obtaining SFR $= (13.4 \pm 1.8) \times [(M_\star/10^{10}\, M_\odot)]^{0.73 \pm 0.09}\, M_\odot$ yr^{-1}; the power-law index shows no change over $z \approx 0.7$–1.45. We find that the nebular line emission suffers less extinction than the stellar continuum, contrary to the situation in the local universe; the ratio of nebular extinction to stellar extinction increases with decreasing redshift. We obtain an upper limit of 0.87 Gyr to the atomic gas depletion time of a subsample of DEEP2 galaxies at $z \approx 1.3$; neutral atomic gas thus appears to be a transient phase in high-z star-forming galaxies.

Key words: galaxies: high-redshift – galaxies: star formation – radio continuum: galaxies

1. Introduction

In recent years, optical imaging and spectroscopic studies of the "deep fields" (e.g., the Hubble Deep Fields, the *Chandra* Deep Field South, the COSMOS field, etc; e.g., Dickinson et al. 2003; Giavalisco et al. 2004; Scoville et al. 2007) have yielded detailed information on the star formation activity in galaxies over a wide range of redshifts (e.g., Madau & Dickinson 2014). Such studies have shown that the comoving star formation rate (SFR) density rises steadily from $z \approx 7$ to $z \approx 3$, is roughly flat over $z \approx 1$–3, and then declines by a factor of 10 from $z \approx 1$ to the present epoch (e.g., Le Floc'h et al. 2005; Hopkins & Beacom 2006; Bouwens et al. 2014). Both the metallicity and the SFR of star-forming galaxies have been found to depend on stellar mass, in the local universe and at high redshifts (e.g., Brinchmann et al. 2004; Tremonti et al. 2004; Erb et al. 2006; Noeske et al. 2007).

The tight relation between SFR and stellar mass in star-forming galaxies (the "main sequence," with SFR $\propto M_\star^\alpha$) and its redshift evolution have been topics of extensive scrutiny over the last decade, with a variety of studies using galaxy samples selected based on different criteria and using different SFR indicators (e.g., Brinchmann et al. 2004; Daddi et al. 2007; Elbaz et al. 2007; Noeske et al. 2007; Salim et al. 2007; Pannella et al. 2009, 2015; Santini et al. 2009; Karim et al. 2011; Whitaker et al. 2014; Tasca et al. 2015). The power-law index and normalization of the main sequence have been shown to play important roles in the evolution of galaxies and their mass functions (e.g., Renzini 2009; Peng et al. 2010).

However, most studies of the main sequence in high-z galaxies are based on SFR estimates from optical imaging or spectroscopy, using rest-frame ultraviolet (UV) or optical

tracers. These are susceptible to dust obscuration effects, and typically only yield the unobscured SFR, uncorrected for dust extinction. Conversely, radio continuum studies allow one to determine the total SFR of galaxies, from both unobscured and obscured star formation, from the tight correlation between the 1.4 GHz radio luminosity and the far-infrared luminosity of star-forming galaxies (e.g., Condon 1992; Yun et al. 2001; Magnelli et al. 2015; Pannella et al. 2015). Calibration relations can then be used to infer the total SFR of a galaxy from its measured rest-frame 1.4 GHz radio luminosity (e.g., Yun et al. 2001; Bell 2003; Kennicutt & Evans 2012).

Unfortunately, deep integrations with current radio telescopes are needed to detect the rest-frame 1.4 GHz continuum emission from normal star-forming galaxies at even low redshifts, $z \approx 0.2$. However, it is possible to infer the *statistical* star formation properties of a sample of galaxies by stacking their 1.4 GHz continuum emission, and then deriving their median (or mean) SFR from the stacked 1.4 GHz radio luminosity (e.g., White et al. 2007). Such studies can then be used to trace the dependence of the median SFR on various galaxy properties, such as metallicity, stellar mass, color, redshift, etc.

Most radio stacking studies in the literature use 1.4 GHz radio continuum images of optical deep fields (e.g., Carilli et al. 2008; Dunne et al. 2009; Pannella et al. 2009, 2015). While this implies a high continuum sensitivity, the stacking for high-z galaxies is effectively being done at a far higher *rest-frame* frequency than 1.4 GHz. One has to then assume a spectral index for the radio emission to infer the rest-frame 1.4 GHz luminosity, and then, the total SFR. We report here deep Giant Metrewave Radio Telescope (GMRT) 610 MHz continuum imaging of four subfields of the DEEP2 Galaxy Redshift Survey (Newman et al. 2013), which allow us to probe the dependence of the SFR on redshift and stellar mass

---

[4] DST Swarnajayanti Fellow.

Table 1
Summary of the Observational Details and Results

	Subfield 1	Subfield 2	Subfield 3	Subfield 4
R.A. (J2000)	$16^h\ 48^m\ 00\overset{s}{.}0$	$16^h\ 51^m\ 00\overset{s}{.}0$	$23^h\ 28^m\ 00\overset{s}{.}0$	$23^h\ 32^m\ 00\overset{s}{.}0$
Decl. (J2000)	$34°56'00\overset{''}{.}0$	$34°56'00\overset{''}{.}0$	$0°9'00\overset{''}{.}0$	$0°9'00\overset{''}{.}0$
Central frequency (MHz)	617.73	617.73	637.73	637.73
On-source time (Hr)	8.5	8.5	13	13
Synthesized beam	$4\overset{''}{.}7 \times 3\overset{''}{.}9$	$5\overset{''}{.}2 \times 4\overset{''}{.}3$	$5\overset{''}{.}9 \times 4\overset{''}{.}6$	$6\overset{''}{.}1 \times 4\overset{''}{.}4$
rms noise (μJy)	21	39	22	14
Stacked galaxies	987	994	936	781

for a near-complete sample of star-forming galaxies at $0.7 \lesssim z \lesssim 1.45$ via stacking of their rest-frame 1–1.4 GHz radio continuum emission.[5]

2. The DEEP2 Survey Fields: GMRT Observations and Data Analysis

The DEEP2 fields (Newman et al. 2013) were chosen as the targets for our GMRT 610 MHz observations (Kanekar et al. 2016). The DEEP2 Survey provides spectroscopic redshifts, using the O II λ3727 doublet, for $\approx$3,800 galaxies at $z \approx 0.7$–1.45 over 2.8 deg^2 area on the sky, and is complete to an apparent magnitude of $R_{AB} = 24.1$ (i.e., an absolute B-band magnitude of $M_B = -20$ at $z \approx 1$; Newman et al. 2013). The values of M_B and U−B from the DEEP2 Survey were used to estimate the stellar masses of the galaxies, assuming a Salpeter initial mass function (IMF) with the calibration of Weiner et al. (2009). Only galaxies with spectroscopic redshifts of quality three or four (i.e., "secure" redshifts, with $\geqslant$95% probability of being correct; see Newman et al. 2013) were included in our analysis.

The GMRT 610 MHz receivers were used in 2012 to observe four of the DEEP2 subfields, with a bandwidth of 33.33 MHz subdivided into 512 channels. Two subfields were observed at a central frequency of 617.73 MHz and two at 637.73 MHz, with total times of $\approx$12–18 hours per subfield (Kanekar et al. 2016). The GMRT primary beam has a full width at half maximum (FWHM) of $\sim$43′ at these frequencies, which covers an entire DEEP2 subfield (36′ × 30′) in a single pointing.

The initial data analysis, including data editing, initial calibration, and self-calibration, was carried out in "classic" AIPS (and is described in detail in Kanekar et al. 2016). The self-calibrated visibilities were then imaged in CASA, using the w-projection algorithm (Cornwell et al. 2008), to produce the final continuum images (including a correction for the shape of the GMRT primary beam). Table 1 summarizes the observational details and results for the four GMRT pointings. These are among the deepest radio continuum images at $\approx$610 MHz in the literature (e.g., Taylor & Jagannathan 2016).

3. Stacking the Radio Continuum

We initially smoothed all four GMRT images with a uniform elliptical Gaussian beam of FWHM = $6\overset{''}{.}1 \times 4\overset{''}{.}8$, which contains the synthesized beams of all the individual subfields. We then estimated the local rms noise in a box of size 50″ × 50″ centered at the location of each DEEP2 galaxy, and

used this to generate the rms noise distribution for each field. This was used to exclude DEEP2 galaxies with high local rms noise, in the upper 10% tail of the rms noise distribution for each field. Varying the exclusion threshold (between 5% and 20%) did not significantly affect our results. We also only included DEEP2 galaxies lying within the FWHM of the GMRT primary beam, to reduce the effect of deconvolution errors, which increase significantly below the half-power point of the primary beam.

It is important to exclude active galactic nuclei (AGNs) from the sample, in order to interpret the stacked radio emission as arising from star formation. Studies of galaxy radio luminosity functions have found that 1.4 GHz radio luminosities $\gtrsim 2 \times 10^{23}$ W Hz^{-1} arise mostly from AGNs, while lower luminosities are produced by star formation (e.g., Condon et al. 2002; Sadler et al. 2002; Smolčić et al. 2008). The 5σ detection threshold in our images ($\approx$70–195 μJy) corresponds to a 1.4 GHz radio luminosity of $\approx(4$–$10) \times 10^{23}$ W Hz^{-1} at the median redshift, $z \approx 1$, of our targets. All individual radio detections are hence likely to arise from AGNs (or from extreme starburst galaxies). To reduce AGN contamination, we hence excluded from the stack any DEEP2 galaxy detected at $\geqslant 5\sigma$ significance with respect to its local rms noise.

We focused on blue, star-forming galaxies, with "color" $C \leqslant 0$, where $C = (U-B) + 0.032\,(M_B + 21.62) - 1.035$ (Willmer et al. 2006). Furthermore, we only considered galaxies with $M_B \leqslant -21$, as this yields a near-complete, absolute-magnitude-limited sample (see Figure 1; Newman et al. 2013). However, we note that the DEEP2 survey is not strictly complete at $M_B \leqslant -21$ over $0.7 \lesssim z \lesssim 1.45$, as there are galaxies in the survey with currently unknown redshifts (e.g., redshift quality <3; Newman et al. 2013).

The stacking was carried out in rest-frame 1.4 GHz luminosity $L_{1.4GHz}$, rather than flux density, to correctly account for the different luminosity distances and redshifts of individual galaxies. This was done by shifting a 50″ × 50″ subimage centered on each galaxy from flux density to $L_{1.4GHz}$, assuming a spectral index of $\alpha = -0.8$ (with flux density $S_\nu \propto \nu^\alpha$; e.g., Condon 1992), before carrying out the stacking procedure. We used "median stacking" as the median is more robust against outliers than the mean, and provides information on "typical" members of the target population (White et al. 2007). The use of median stacking reduces the effect of contamination by undetected radio emission (e.g., lying just below our 5σ detection threshold) from individual AGNs or starburst galaxies. Finally, the stacking was carried out using 50″ × 50″ subimages, centered at the galaxy locations; the same procedure was used to stack regions 100″ away from the galaxies, to test for systematic effects.

---

[5] We will assume a flat Λ-cold-dark-matter cosmology, with $H_0 = 67.8$ km s^{-1} Mpc^{-1}, $\Omega_m = 0.31$, and $\Omega_\Lambda = 0.69$ (Ade et al. 2016).
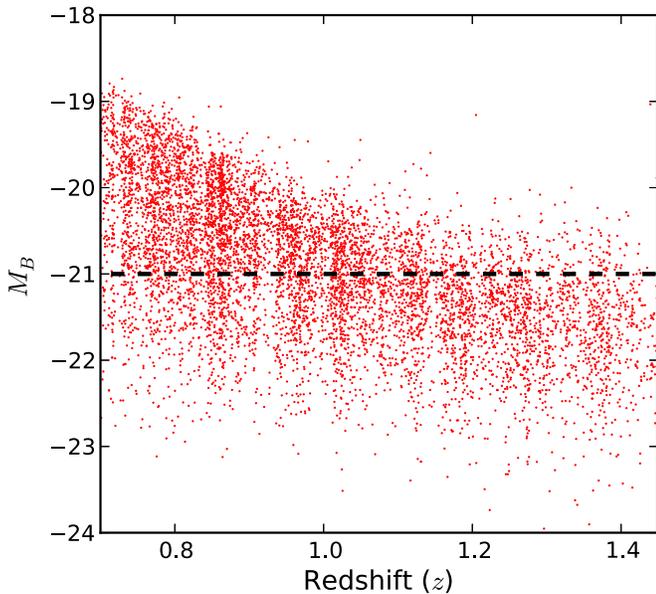
Figure 1. Rest-frame absolute B-band magnitudes of the DEEP2 galaxies within the FWHM of the GMRT images. We retain galaxies with $M_B \leqslant -21$ in our stacking analysis, to obtain a complete sample out to $M_B \leqslant -21$ over our entire redshift range.

4. Results and Discussion

4.1. The Total SFR of the DEEP2 Galaxies

Our sample contains 3698 blue star-forming galaxies with $M_B \leqslant -21$, a median redshift $z_{med} = 1.1$, and a median stellar mass $M_\star = 10^{10.3} M_\odot$. Figure 2(A) shows the median-stacked image of these galaxies: an unresolved source, detected at $\approx 17\sigma$ significance with $L_{1.4GHz} = (4.13 \pm 0.24) \times 10^{22} \, W \, Hz^{-1}$, is clearly visible. Figure 2(B) shows the image obtained from stacking locations offset by $100''$ from the DEEP2 galaxies; this shows no evidence of either emission or systematic effects.

To obtain the total SFR from the 1.4 GHz luminosity, we adopt the calibration of Yun et al. (2001),

$$\mathrm{SFR}(M_\odot \, yr^{-1}) = (5.9 \pm 1.8) \times 10^{-22} \, L_{1.4 \, GHz}(W \, Hz^{-1}), \quad (1)$$

which assumes a Salpeter IMF, with masses in the range $(0.1-100) M_\odot$. The $\approx 30\%$ uncertainty in this relation arises primarily from estimates of the local SFR density (Yun et al. 2001); this systematic uncertainty has not been included in our error estimates below. Using our measured rest-frame 1.4 GHz luminosity in Equation (1) yields a median SFR of $\mathrm{SFR_{RADIO}} = (24.4 \pm 1.4) \, M_\odot \, yr^{-1}$ for the 3698 galaxies of our sample.

The fact that the stacked radio emission is unresolved implies a transverse size $\lesssim 8$ kpc at $z_{med} = 1.1$. Note that any uncorrected phase errors arising from the ionosphere would increase the observed spatial extent of the radio emission. Star formation in the DEEP2 galaxies thus appears to typically arise from the central regions, of size $\ll 8$ kpc.

4.2. SFR Evolution with Redshift

We examined the dependence of the SFR and the specific star formation rate (sSFR, defined as the SFR per unit stellar mass) on redshift by dividing the sample into six uniformly spaced redshift

bins covering $z \approx 0.7-1.45$, and carrying out the median stacking independently for the galaxies in each bin. For the sSFR, the stacking was carried out in the ratio $L_{1.4 \, GHz}/M_\star$ for each galaxy, so as to not introduce errors from averaging in the stellar mass. Figures 3(A) and (B) show, respectively, the median SFR and the median sSFR of each subsample plotted against the median redshift of its bin. We find that both the SFR and the sSFR decrease with decreasing redshift, with $\mathrm{SFR} \propto (1+z)^{1.98 \pm 0.50}$ and $\mathrm{sSFR} \propto (1+z)^{3.94 \pm 0.57}$ over $0.7 \lesssim z \lesssim 1.45$. This is consistent with earlier studies, mostly based on optical SFR indicators, which have obtained $\mathrm{sSFR} \propto (1+z)^\beta$ with $\beta \approx 2.8-3.8$ for $0 < z \lesssim 2.5$ (e.g., Karim et al. 2011; Fumagalli et al. 2014; Ilbert et al. 2015; Tasca et al. 2015). We note that median SFR of our galaxies increases less steeply with redshift than the median sSFR because the median stellar mass of the sample decreases with increasing redshift (see also Sklias et al. 2017, for *Herschel*-detected galaxies at $1.2 < z < 4$).

To study the SFR evolution of galaxies with similar stellar mass, we chose subsamples of the DEEP2 galaxies in two different mass ranges, $10.3 < \log[M_\star/M_\odot] < 10.7$ and $\log[M_\star/M_\odot] > 10.7$. The mass ranges were chosen to ensure that the median stellar mass of each subsample is approximately equal in each redshift bin. Figures 4(A) and (B) show the redshift evolution of SFR and sSFR, respectively, for galaxies in the above mass ranges. We find that the SFR increases with redshift as $\mathrm{SFR} \propto (1+z)^{1.83 \pm 0.53}$ and $\mathrm{SFR} \propto (1+z)^{3.53 \pm 0.72}$ for, respectively, the lower-mass ($10.3 < \log[M_\star/M_\odot] < 10.7$) and higher-mass ($\log[M_\star/M_\odot] > 10.7$) subsamples, while the sSFR increases $\propto (1+z)^{2.02 \pm 0.42}$ (low-mass subsample) and $\propto (1+z)^{3.49 \pm 0.94}$ (high-mass subsample). We thus find only marginal ($\approx 2\sigma$ significance) evidence that the SFR increases more steeply with redshift for the higher-mass subsample in our data. Indeed, excluding the last redshift bin from our fits reduces the statistical significance of the difference in the exponents of the two subsamples further, to $\approx 1\sigma$ significance. We thus find no statistically significant evidence of a difference in the redshift evolution of the SFR for low-mass and high-mass galaxies, with stellar masses $\log[M_\star/M_\odot] > 10.3$ in the redshift range $0.7 \lesssim z \lesssim 1.45$.

We note, in passing, that the DEEP2 galaxy sample is not complete in stellar mass. As such, it is possible that massive dusty galaxies with high SFRs have been excluded from our stellar mass subsamples due to dust obscuration. This effect is likely to vary with redshift as the observed optical bands translate to shorter rest-frame UV wavelengths at higher redshifts, with correspondingly higher dust extinction effects. Any dependence of the mass completeness of the sample on redshift, if present in our sample, is likely to affect our results.

4.3. The Main Sequence of Star-forming Galaxies

Next, we studied the dependence of the SFR on $M_\star$ by stacking galaxy subsamples binned by stellar mass. Figure 5(A) shows the median SFR of each subsample plotted against its median $M_\star$: a tight correlation between SFR and $M_\star$ (usually referred to as the "main sequence"; e.g., Noeske et al. 2007) is clear in the figure, with $\mathrm{SFR} = (13.4 \pm 1.8) \times [M_\star/(10^{10} \, M_\odot)]^{(0.73 \pm 0.09)} \, M_\odot \, yr^{-1}$. Our main-sequence power-law index of $\alpha \approx 0.73 \pm 0.09$ is in good agreement with earlier studies at similar redshifts ($z \approx 0.5-2.5$), which have typically obtained $\alpha \approx 0.6-0.9$ (e.g., Elbaz et al. 2007; Noeske et al. 2007; Santini et al. 2009; Pannella et al. 2015).

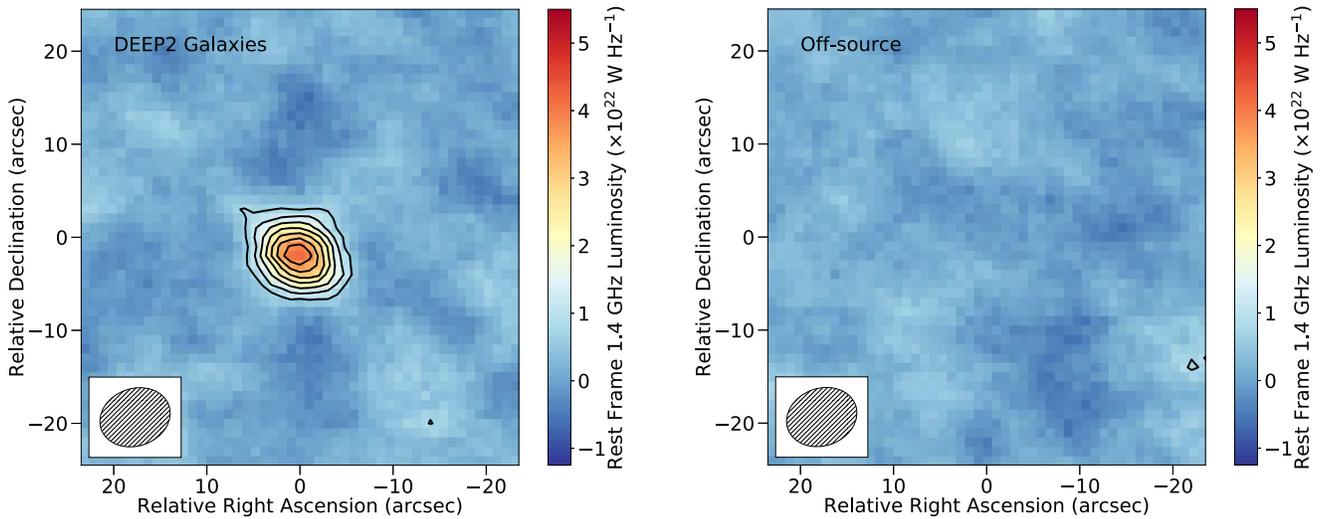**Figure 2.** Stacked rest-frame 1.4 GHz radio continuum luminosity (in units of 10^{22} W Hz^{-1}) from (A, left panel) the 3698 blue star-forming galaxies with $M_B \leqslant -21$ of our sample, and (B, right panel) locations offset by $100''$ from the 3698 DEEP2 galaxies. The rms noise on each image is $\approx 2.5 \times 10^{21}$ W Hz^{-1}. A point source is clearly detected at the center of the left panel, while the right panel shows no evidence for emission.

Whitaker et al. (2014) studied the main-sequence relation for mass-complete samples at different redshift intervals in the range $0.5 < z < 2.5$, finding evidence for a flattening of the slope of the main sequence at high stellar masses in all redshift bins. Our main-sequence relation at $z_{\mathrm{med}} = 1.1$ is in good agreement with the relation obtained by Whitaker et al. (2014) at $z \approx 1.25$. However, our sensitivity is too low to confirm the presence of a changing slope in the main sequence.

We examined the evolution of the main sequence with redshift by dividing the full sample into two redshift bins ($0.7 < z < 1.0$ and $1.0 < z < 1.45$), and then independently applying the median stacking procedure to six stellar mass bins within each redshift bin. Figure 5(B) shows the median SFR plotted against the median $M_\star$ for galaxies in the high-z and low-z subsamples, indicated by filled squares and circles, respectively. We obtained SFR = $(10.7 \pm 2.3) \times [M_\star/(10^{10} M_\odot)]^{(0.70\pm0.15)} M_\odot$ yr^{-1} for the low-z subsample ($z_{\mathrm{med}} \approx 0.85$) and SFR = $(17.3 \pm 2.1) \times [M_\star/(10^{10} M_\odot)]^{(0.77\pm0.09)} M_\odot$ yr^{-1} for the high-z subsample ($z_{\mathrm{med}} \approx 1.20$). We thus find only weak ($\approx 2\sigma$ significance) evidence that the normalization of the main sequence increases with increasing redshift, by a factor of ≈ 1.6 between $z \approx 0.85$ and $z \approx 1.2$. Similar results have been obtained in earlier studies, albeit mostly using either optical SFR indicators (e.g., Noeske et al. 2007), or galaxy samples with photometric redshifts (e.g., Santini et al. 2009; Pannella et al. 2015). However, we find no evidence that the slope of the main sequence evolves with redshift, over $0.7 \lesssim z \lesssim 1.45$, contrary to the expected decline in slope with time expected in cosmic downsizing scenarios (Cowie et al. 1996), due to the shifting of star formation activity from more-massive to less massive galaxies with time (see also Santini et al. 2009; Pannella et al. 2015).

Our main-sequence relation at $z \approx 1.25$ is consistent within the errors with the relation obtained by Whitaker et al. (2014) at the same redshift. However, our relation at $z \approx 0.85$ is significantly above that of Whitaker et al. (2014) at $z \approx 0.75$. This is consistent with a decline in the normalization of the main sequence with decreasing redshift (e.g., Elbaz et al. 2007), as the two low-z subsamples have different redshift distributions, $0.5 < z < 1.0$ for Whitaker et al. (2014) and $0.7 < z < 1.0$ for this work.

However, we again note that the DEEP2 galaxies are selected to have $R < 24.1$, i.e., they are selected at rest-frame wavelengths of ≈ 2700–3800 Å, and that the sample is not mass complete. Massive dusty galaxies with high SFRs are likely to have been excluded due to their high extinction. Our "color" selection also excludes some of these galaxies as these are likely to be red in color. This might affect our results by flattening the slope of the main sequence. The effect is likely to be stronger for higher-redshift galaxies, as these are selected at rest-frame UV wavelengths, <3000 Å, where the extinction effects are larger. This could cause our inferred main-sequence slopes to appear flatter, especially in the high-z subsample.

4.4. Comparisons with SFRs from Other Tracers: Dust Extinction

The SFRs of high-z star-forming galaxies, such as the DEEP2 galaxies of our sample, are usually estimated from optical or near-IR imaging or spectroscopy, based on SFR tracers such as the rest-frame UV continuum luminosity or the [O II]$\lambda3727$ or Hα line luminosity. However, the measured luminosities in these SFR tracers are reduced from their intrinsic values due to extinction by dust in the interstellar medium of the target galaxy. The use of such tracers hence usually underestimates the SFR in high-z galaxies. A variety of prescriptions are available in the literature to correct for the dust attenuation (e.g., Salim et al. 2007; Hao et al. 2011), but their accuracy is unknown, as dust extinction effects are likely to depend on the physical properties of the galaxies (e.g., stellar mass, color, metallicity, etc). In the case of the DEEP2 galaxy sample, we have estimated the median *total* SFR (i.e., both unobscured and obscured) from the rest-frame 1.4 GHz radio continuum, which is unaffected by dust extinction. In this section, we estimate the SFRs of different subsamples of the DEEP2 galaxies from a set of optical/UV tracers that are commonly used for high-z galaxies (the near-ultraviolet (NUV) continuum luminosity, the rest-frame U-band continuum luminosity, and the [O II]$\lambda3727$ line luminosity). We then compare
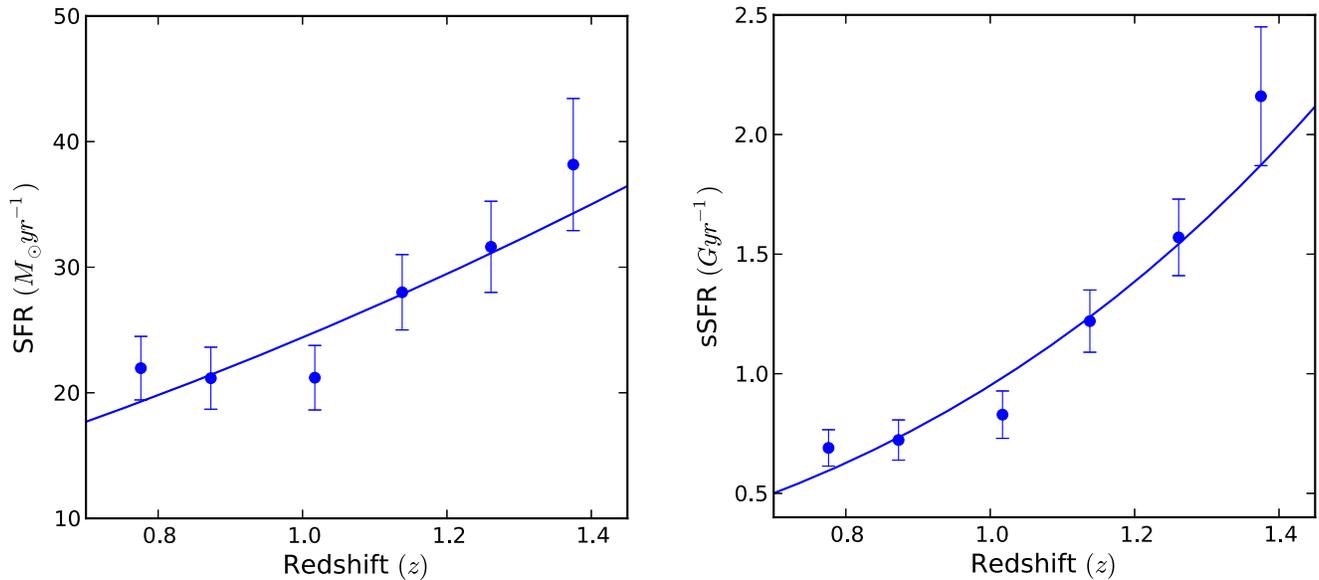
Figure 3. Redshift evolution of (A) the SFR (left panel) and (B) the sSFR (right panel) for the 3698 blue star-forming galaxies of our sample. The solid curves show the best-fit power-law models for the redshift evolution, with SFR $\propto (1 + z)^{1.98 \pm 0.50}$ and sSFR $\propto (1 + z)^{3.94 \pm 0.57}$.

these median SFR estimates to the radio-derived median SFRs to infer the correction for dust extinction that should be applied to the SFR inferred from each tracer for similar populations of star-forming galaxies, as a function of color, stellar mass, and redshift. The SFR correction factor will be referred to as the dust extinction correction factor ϵ, defined as

$$\epsilon_X \equiv \text{SFR}_{\text{RADIO}}/\text{SFR}_X, \qquad (2)$$

where X corresponds to the SFR tracer in question (i.e., the NUV continuum luminosity, the U-band continuum luminosity, the [O II]$\lambda3727$ line luminosity, etc.), and $\epsilon_X \geqslant 1$.

The [O II]$\lambda3727$ line luminosity is a popular SFR tracer in high-z galaxies, especially for objects at $z \approx 0.7$–2.5, for which the Hα line is redshifted to near-IR wavelengths. In the case of the DEEP2 galaxies of our sample, reliable [OII]$\lambda3727$ line luminosities are available for galaxies at $0.8 < z < 1.4$, and one can hence immediately infer the SFR for these galaxies from this tracer, using standard calibrations (e.g., Kennicutt 1998). Following Weiner et al. (2007), we assume a line ratio [O II]$\lambda3727/H_\alpha = 0.69$, appropriate for high-redshift galaxies. We then apply the calibration (valid for a Salpeter IMF; Kennicutt 1998)

$$[\text{SFR}_{\text{O II}}/M_\odot \text{ yr}^{-1}] = 7.9 \times 10^{-42}[L_{H\alpha}/\text{erg s}^{-1}], \qquad (3)$$

to obtain a median SFR of $\text{SFR}_{\text{O II}} = 12.5 \, M_\odot \text{ yr}^{-1}$. Combining this with our median radio SFR estimate yields a median dust extinction correction factor of $\epsilon_{\text{O II}} \approx 2.0$ for the [O II] $\lambda3727$ SFR estimator. We emphasize that this correction factor is applicable for main-sequence, star-forming galaxies with $M_B \leqslant -21$.

Next, the observed B-band magnitudes of our 3698 target galaxies are available from the DEEP2 survey. Since the sample galaxies lie in the redshift range $0.7 \lesssim z \lesssim 1.45$, the observed-frame B-band corresponds to rest-frame emission wavelengths 180–260 nm, i.e., at NUV wavelengths. About 90% of the NUV continuum emission of a galaxy is provided by young stars (of ages below 200 Myr; Kennicutt & Evans 2012). The rest-frame 230 nm NUV luminosity of a galaxy can hence be used to infer its SFR (e.g., Hao et al. 2011;

Murphy et al. 2011; Kennicutt & Evans 2012), via the relation (applicable for a Kroupa IMF; Kroupa & Weidner 2003)

$$\log\left(\frac{\text{SFR}_{\text{NUV}}}{M_\odot \text{ yr}^{-1}}\right) = \log\left(\frac{\nu L_\nu}{\text{erg s}^{-1}}\right) - 43.17. \qquad (4)$$

Assuming that this calibration applies to the rest-frame wavelength range of 180–260 nm (note that the calibration is in $\nu \times L_\nu$ and hence the above assumption is good to first order), we apply it to the observed-frame B-band luminosities, to obtain a median SFR (after adding 0.15 dex to shift to a Salpeter IMF) of $\text{SFR}_{\text{NUV}} = 5.2 \, M_\odot \text{ yr}^{-1}$. Comparing our median radio SFR with this median NUV SFR then yields $\epsilon_{\text{NUV}} \approx 4.7$, for star-forming galaxies with $M_B \leqslant -21$.

The DEEP2 survey also provides the rest-frame U-band ($\lambda \approx 3600$ Å) absolute magnitude of our target galaxies (Newman et al. 2013). The rest-frame U-band continuum luminosity can be used to estimate the SFR following the prescription of Hopkins et al. (2003),

$$\log\left(\frac{\text{SFR}_U}{M_\odot \text{ yr}^{-1}}\right) = 1.186 \times \log\left(\frac{L_U}{1.81 \times 10^{21} \text{ W Hz}^{-1}}\right), \qquad (5)$$

which assumes a Salpeter IMF. This yields a median SFR of $\text{SFR}_U = 9.6 \, M_\odot \text{ yr}^{-1}$. Combining this U-band median SFR estimate with our median radio SFR then yields a dust extinction correction factor of $\epsilon_U \approx 2.5$ for the U-band SFR, again for star-forming galaxies with $M_B \leqslant -21$.

We thus find that the largest dust extinction correction factor is needed for the NUV 230 nm continuum luminosity, with $\epsilon_{\text{NUV}} \approx 4.7$; the dust correction factors are similar for the rest-frame U-band continuum luminosity ($\epsilon_U \approx 2.5$) and for the [O II]$\lambda3727$ line luminosity ($\epsilon_{\text{O II}} \approx 2.0$).

We also examined the dependence of the dust extinction correction factor for the NUV-, U-band-, and O II-based SFR estimators on redshift, absolute B-band magnitude, color, and stellar mass. To examine the dependence of ϵ_X on absolute B-band magnitude, we compared the dust extinction correction factors for galaxies with $M_B \leqslant -20$ with the above estimates

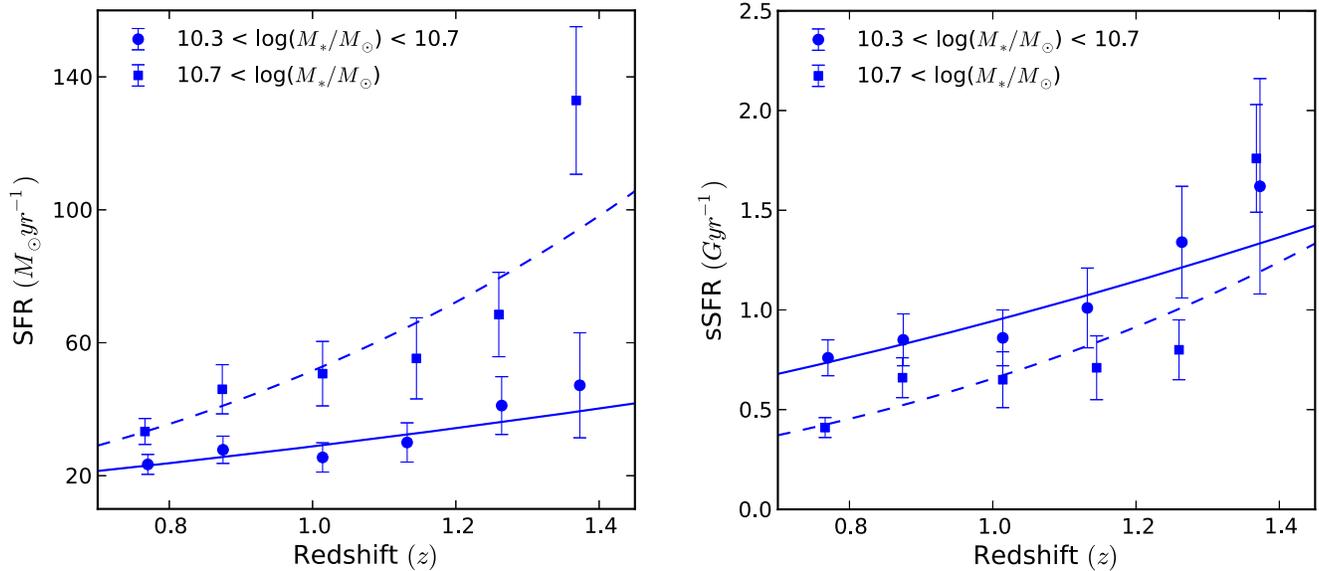**Figure 4.** Redshift evolution of (A) the SFR (left panel) and (B) the sSFR (right panel) for DEEP2 galaxies in two stellar mass ranges, $10.3 < \log[M_\star/M_\odot] < 10.7$ and $\log[M_\star/M_\odot] > 10.7$. For both mass ranges, the median stellar mass in the different redshift bins is approximately the same. The solid and dashed curves show the best-fit power-law models for the two different mass ranges. The power-law exponents for the SFR evolution are 1.83 ± 0.53 and 3.53 ± 0.72 for, respectively, $10.3 < \log[M_\star/M_\odot] < 10.7$ and $\log[M_\star/M_\odot] > 10.7$, while the exponents for the sSFR evolution are 2.02 ± 0.42 and 3.44 ± 0.94, respectively.

of ϵ_X for $M_B \leqslant -21$. To do this, we restricted to the redshift range $0.7 < z < 1.0$, for which the DEEP2 sample is complete down to $M_B \leqslant -20$ (Newman et al. 2013). Including all DEEP2 galaxies with $M_B \leqslant -20$ and restricting the redshift range to $0.7 < z < 1.0$, we obtained dust extinction correction factors of $\epsilon_{NUV} \approx 3.9$, $\epsilon_U \approx 2.5$, and $\epsilon_{O\,II} \approx 1.6$. In the same redshift range, for $M_B \leqslant -21$, we obtain $\epsilon_{NUV} \approx 5.0$, $\epsilon_U \approx 2.4$, and $\epsilon_{O\,II} \approx 2.2$. The dust extinction correction factor thus appears to be systematically larger for brighter galaxies, except for the calibration based on the U-band luminosity.

Figure 6(A) shows the dependence of ϵ_X on redshift for the three SFR tracers. We find no evidence that the dust extinction correction factor varies with redshift over $0.7 < z < 1.45$, for galaxies with $M_B \leqslant -21$. Figures 6(B) and (C) plot ϵ_X against galaxy color and stellar mass, respectively, for the three SFR tracers. ϵ_X is seen to increase with both increasing color (i.e., from bluer to redder galaxies) and increasing stellar mass for all three estimators, with a strong dependence on color and stellar mass for the NUV luminosity and the $[O\,II]\lambda3727$ line luminosity, and a weaker dependence for the rest-frame U-band luminosity. This is unsurprising for the NUV emission, given that dust attenuation is most effective at shorter wavelengths. The $[O\,II]\lambda3727$ line emission suffers relatively little dust extinction in bluer and less massive galaxies, but is strongly affected by attenuation effects in redder and more-massive galaxies, making it a good tracer of the total SFR for blue galaxies with $M_\star \leqslant 10^{10.4} M_\odot$, but a less reliable tracer for more-massive galaxies.

Finally, the dust extinction correction factor for the SFR estimate from the rest-frame U-band luminosity shows a relatively weak dependence on color and stellar mass, with ϵ_U varying by less than a factor of ≈ 2 over our color and stellar mass range. Furthermore, we find no evidence that ϵ_U varies with redshift (over $0.7 < z < 1.45$) or B-band absolute magnitude (comparing galaxies with $M_B \leqslant -20$ with those with $M_B \leqslant -21$, in the same redshift range). After applying an average dust extinction correction factor of $\epsilon_U \approx 2.5$, the rest-frame U-band luminosity thus appears to yield a reasonable

tracer of the total SFR for blue, star-forming, main-sequence galaxies at $z \approx 0.7$–1.5.

We emphasize that the U-band luminosity of a galaxy is only likely to be a good tracer of the SFR for galaxies dominated by young stellar populations (e.g., Cram et al. 1998; Hopkins et al. 2003). Moreover, the U-band luminosity is known to depend on both the evolutionary timescale and the star formation history (e.g., Bell 2003; Hopkins et al. 2003), yielding a nonlinear relation between the SFR and the U-band luminosity (Hopkins et al. 2003). Specifically, the U-band luminosity may be contaminated by emission from older stellar populations, especially in low-luminosity galaxies. As such, caution should be used when inferring the SFR from the rest-frame U-band luminosity. Despite these caveats, the fact that the dust extinction correction factor for the SFR estimate from the U-band luminosity does not vary significantly with color, stellar mass, B-band absolute magnitude, or redshift for the subsample of DEEP2 galaxies with $M_B \leqslant -21$, indicates that the rest-frame U-band luminosity may be an interesting tracer of the SFR in similar galaxies at $z \approx 1$.

4.5. Nebular and Stellar Extinction

In the local universe, nebular emission lines have been shown to suffer more extinction, by a factor of ≈ 1.7, than the stellar continuum at the same wavelength in a wide range of galaxy types (e.g., Fanelli et al. 1988; Calzetti et al. 1994; Mayya & Prabhu 1996; Calzetti 1997; Sullivan et al. 2001; Cid Fernandes et al. 2005; Wild et al. 2011). This differential extinction has been shown to depend on galaxy properties such as the SFR, the sSFR, the inclination, etc. (e.g., Sullivan et al. 2001; Cid Fernandes et al. 2005; Wild et al. 2011; Battisti et al. 2016, 2017). A two-component dust model, including a diffuse, optically thin component arising from the galactic interstellar medium and a dense, optically thick component in the "birth-clouds" of actively star-forming regions, has been proposed to explain the excess attenuation suffered by the nebular emission (Calzetti et al. 1994; Charlot & Fall 2000).
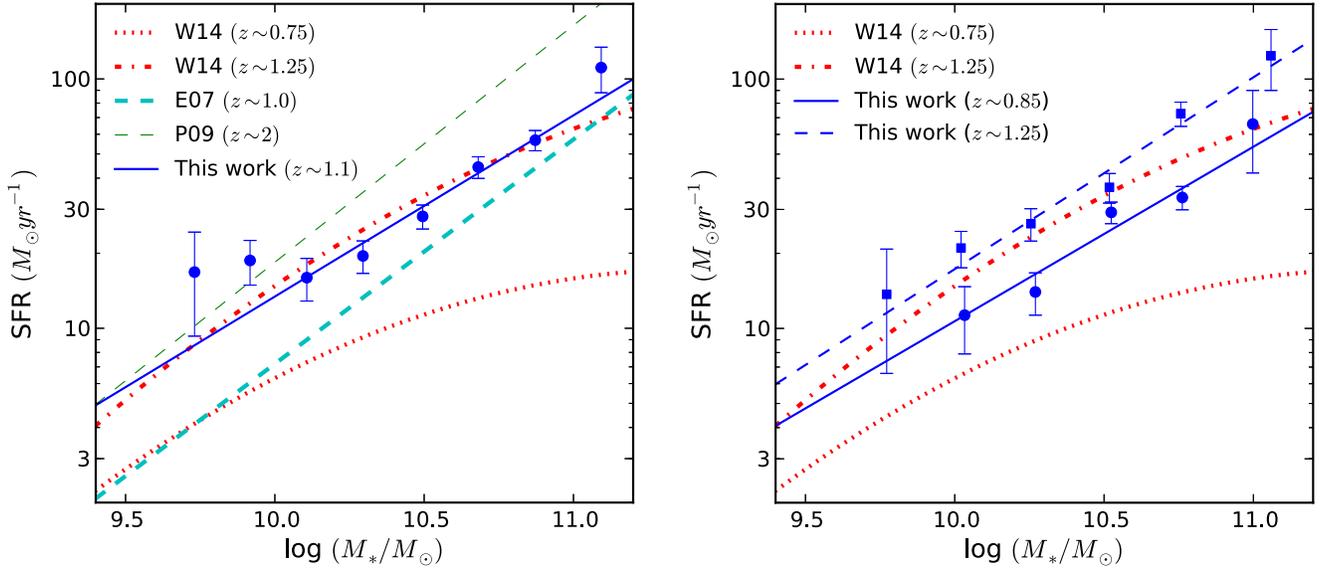
Figure 5. (A) The "main sequence," with median SFR plotted vs. median stellar mass for the 3698 galaxies of our full sample; the best-fit main-sequence relation is shown by the solid blue line. The main-sequence relations obtained by Elbaz et al. (2007, E07; cyan dashed line, at $z \approx 1$), Pannella et al. (2009, P09; black dashed line, at $z \approx 2$), and Whitaker et al. (2014, W14; red dotted and dashed–dotted curves, for redshift bins centered at $z \approx 0.75$ and $z \approx 1.25$, respectively) are also shown, for comparison. (B) The redshift evolution of the main sequence, with the low-z ($0.7 < z < 1.0$) subsample indicated by circles, and the high-z ($1.0 < z < 1.45$) subsample by squares. The solid and dashed blue lines indicate our main-sequence relations for the low-z and high-z subsamples, respectively, while the relations of Whitaker et al. (2014) at $z \approx 0.75$ and $z \approx 1.25$ are again shown as red dotted and dashed–dotted curves, respectively. See the main text for a discussion.

Nebular emission is expected to arise from ionized gas located close to young, hot, ionizing stars within the dense birth-clouds (i.e., is spatially associated with the optically thick dust component), while stellar emission arises from stars both in such regions and throughout the disk; this is expected to be the reason for the higher extinction affecting the nebular emission.

While it is clear that nebular emission is significantly more extincted than the stellar continuum in local star-forming galaxies, the situation is much more unclear at high redshifts. For example, similar extinction factors have been obtained for nebular line and stellar continuum emission in UV-selected galaxies at $z \approx 2$ (e.g., Erb et al. 2006; Reddy et al. 2010) and in far-IR-selected main-sequence galaxies at $z \approx 0.79$–1.5 (Puglisi et al. 2016), while higher extinction of the nebular emission (similar to or even larger than that in the local universe) has been obtained in samples of optical- and near-IR-selected galaxies at $z \approx 1$–2 (e.g., Förster Schreiber et al. 2009; Kashino et al. 2013; Wuyts et al. 2013; Price et al. 2014). Pannella et al. (2015) also found evidence for redshift evolution in the differential extinction of nebular and stellar emission in their sample of sBzK galaxies, with similar extinction factors at high redshifts (out to $z \approx 3$) and higher extinction of the nebular emission (albeit by a lower factor, ≈ 1.3, than that seen in the local universe) at $z \approx 1$. Finally, given that it is possible that the results may depend on galaxy type, we note that Price et al. (2014) obtained a higher attenuation (by a factor of ≈ 1.8) for the nebular emission in a sample of 163 main-sequence star-forming galaxies at $z \approx 1.36$–1.5.

In the previous section, we estimated the dust extinction factors in the DEEP2 galaxies for three UV/optical SFR indicators, the nebular [O II] $\lambda 3727$ line, and the stellar NUV (≈ 230 nm) and U-band (≈ 360 nm) continua. Here, we compare the extinction of nebular emission with that of stellar emission in the DEEP2 galaxies; for this, we use the SFR estimate from the U-band continuum, as its wavelength (≈ 3600 Å) is very similar to that of the [O II] $\lambda 3727$ line. The

dust extinction factor $\epsilon(\lambda)$ is the ratio of the intrinsic luminosity $F_{int}(\lambda)$ to the observed luminosity $F_{obs}(\lambda)$, and is hence related to the color excess [$E(B-V)$] and the reddening curve [$k(\lambda)$] by (e.g., Calzetti et al. 2000)

$$\epsilon(\lambda) = \frac{F_{int}(\lambda)}{F_{obs}(\lambda)} \equiv 10^{0.4.E(B-V).k(\lambda)}. \quad (6)$$

The ratio of the logarithms of the dust extinction factors for the [O II] $\lambda 3727$ line emission and the U-band continuum is then

$$E_{\text{O II/U}} = \frac{\log(\epsilon_{\text{O II}})}{\log(\epsilon_{\text{U}})} \equiv \frac{E_{gas}(B-V).k(373 \text{ nm})}{E_{star}(B-V).k(360 \text{ nm})}$$
$$\approx \frac{E_{gas}(B-V)}{E_{star}(B-V)}, \quad (7)$$

where we have assumed $k(\lambda = 373 \text{ nm}) \approx k(\lambda = 360 \text{ nm})$. We obtain $E_{\text{O II/U}} \approx E_{gas}(B-V)/E_{star}(B-V) = (0.76 \pm 0.04)$ for the DEEP2 galaxies with $M_B \leqslant -21$, over $0.7 < z < 1.4$. The fact that $E_{\text{O II/U}} < 1$ in our sample indicates that the nebular emission in the DEEP2 galaxies suffers *less* extinction than the stellar continuum at a similar wavelength. This is very different from the situation in nearby galaxies (where the ratio is ≈ 1.7) and is also qualitatively different from the results obtained in earlier studies of high-z galaxies, which found either higher extinction of the nebular emission (e.g., Price et al. 2014) or comparable extinctions for the nebular and stellar emission (e.g., Förster Schreiber et al. 2009; Puglisi et al. 2016).

We emphasize that our earlier caveat that the measured rest-frame U-band continuum luminosity might contain contributions from old stars does not affect the above conclusion. Contamination of the U-band continuum by emission from old stars would imply that our U-band SFR estimate is an upper limit, i.e., that our estimate of the dust extinction factor for the U-band stellar continuum is a *lower* limit. This then implies that our estimate of $E_{\text{O II/U}}$ is an upper limit to the true value. In
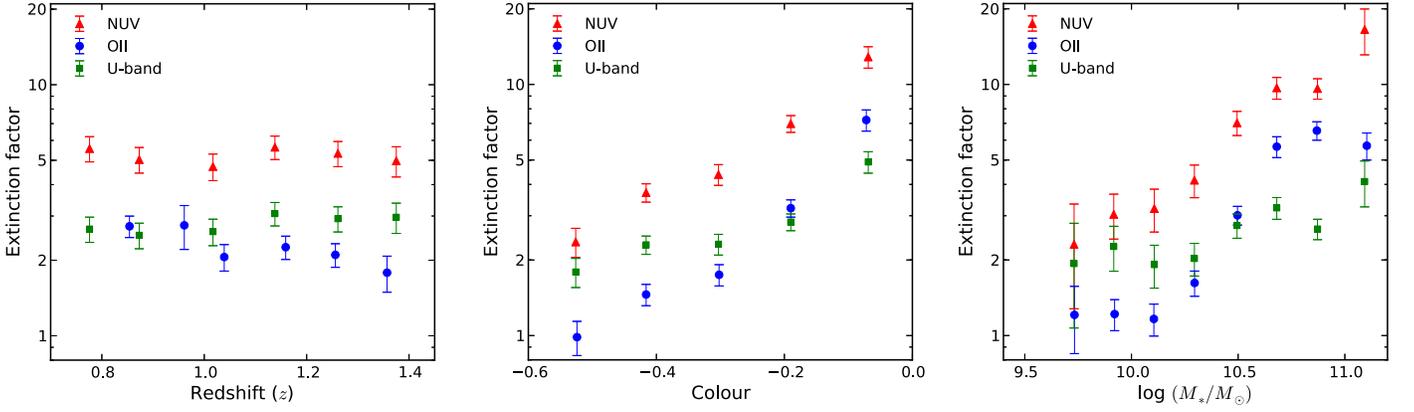
Figure 6. Dust extinction correction factors for the rest-frame 230 nm NUV continuum luminosity (triangles), the rest-frame U-band continuum luminosity (squares), and the [O II]λ3727 line luminosity (circles) plotted against (A, left panel) redshift, (B, middle panel) galaxy color, and (C, right panel) stellar mass, for the 3698 DEEP2 galaxies in our sample with $M_B \leqslant -21$. See the main text for a discussion.
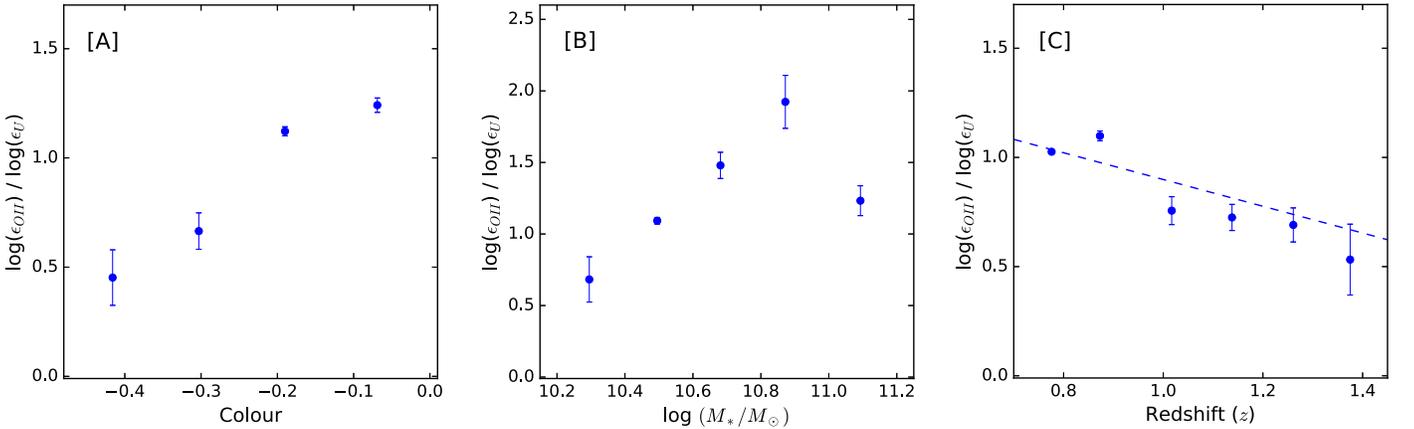

Figure 7. Ratio of the extinction factor for the O II λ3727 Å line to that of the U-band continuum ($E_{OII/U}$) plotted against (A) galaxy color, (B) stellar mass, and (C) redshift, for the DEEP2 galaxies with $M_B \leqslant -21$. The dashed line in the third panel shows the linear fit $E_{O\,II/U} = (1.51 \pm 0.24) - (0.61 \pm 0.30) \times z$. See the main text for a discussion.

other words, the possibility of contributions from an old stellar population to the U-band luminosity can only reduce the inferred value of $E_{O\,II/U}$, and hence does not affect our conclusion that the nebular emission in the DEEP2 galaxies of our sample suffers less extinction than the stellar emission.

The three panels of Figure 7 plot the ratio $E_{O\,II/U} \approx E_{gas}(B-V)/E_{star}(B-V)$ as a function of color, stellar mass, and redshift. The right and middle panels of the figure show that higher values of $E_{O\,II/U}$ are obtained in redder and more-massive galaxies: nebular emission in redder and more-massive galaxies thus appears to suffer larger extinction (relative to the stellar continuum) than similar emission in bluer and less massive galaxies (see also Puglisi et al. 2016). Furthermore, the [O II] λ3727 emission in the reddest and most massive galaxies shows significantly larger extinction than the U-band stellar continuum. Both of these are consistent with a scenario in which larger amounts of the second dust component (assuming a two-component dust model similar to that of Charlot & Fall 2000) are present in the actively star-forming regions in dusty, massive galaxies, and that this second dust component is less prevalent or absent in blue galaxies.

Figure 7(C) shows that the ratio $E_{O\,II/U}$ increases with decreasing redshift in the DEEP2 galaxies, over $1.4 \gtrsim z \gtrsim 0.7$. The dashed straight line shows the best linear fit to the data; we obtain $E_{O\,II/U} = (1.51 \pm 0.24) - (0.61 \pm 0.30) \times z$. Using this relation to extrapolate to lower redshifts, we obtain

$E_{O\,II/U} \approx E_{gas}(B-V)/E_{star}(B-V) = (1.51 \pm 0.24)$ at $z = 0$. Interestingly, this is consistent with the estimates of the excess extinction (a factor of ≈ 1.7) suffered by nebular emission in local star-forming galaxies (e.g., Calzetti et al. 1994, 2000; Cid Fernandes et al. 2005). In the context of the two-component dust model, this suggests that the optically thick dust component steadily builds up in actively star-forming regions of main-sequence galaxies, causing a steady increase in the excess attenuation suffered by the nebular emission relative to the stellar continuum.

To address the possibility that the U-band continuum luminosity might not be a good tracer of the SFR, we have also carried out the analysis via a different approach, using the dust extinction factor estimated from the NUV 230 nm continuum luminosity. To estimate the dust extinction factor for the stellar continuum at 373 nm (i.e., at the wavelength of the O II λ3727 line), we need to know the extinction curve of the DEEP2 galaxies. Since this is not known, we use a range of local extinction curves [$k(\lambda)$], for the Milky Way (Cardelli et al. 1989), Large and Small Magellanic Clouds (LMC and SMC, respectively; Gordon et al. 2003), and local starburst galaxies (Calzetti et al. 1994). These yield $E_{O\,II/373nm} \approx E_{gas}(B-V)/E_{star}(B-V) = (0.63-0.93)$, with the lowest and highest values for the extinction curves of the local starbursts and the SMC, respectively. Note that our result based on using the U-band luminosity as an SFR indicator lies in the

middle of these estimates. We also continue to find that the ratio $E_{\rm O\,II/373nm}$ increases with decreasing redshift, over $1.4 \gtrsim z \gtrsim 0.7$. Extrapolating to lower redshifts for each assumed reddening curve, we obtain $E_{\rm O\,II/373nm} \approx 1.3$–$1.9$ at $z = 0$ (again with the lowest and highest values for the extinction curves of local starbursts and the SMC, respectively), broadly consistent with estimates of the excess extinction suffered by nebular emission in local galaxies. We thus find no evidence that our conclusions might be affected by our use of the U-band continuum luminosity as an SFR indicator.

4.6. The Atomic Gas Depletion Timescale

The timescale on which neutral gas is depleted by star formation, and its dependence on redshift, stellar mass, etc., is a subject of much interest in studies of galaxy evolution (e.g., Schiminovich et al. 2010; Saintonge et al. 2011, 2013; Tacconi et al. 2013; Genzel et al. 2015; Schinnerer et al. 2016). If star formation activity is to be maintained in a galaxy beyond its gas depletion timescale, the gas content must be replenished, probably by accretion of gas from the intergalactic medium. Most studies of the gas depletion timescale in high-z, star-forming galaxies have focussed on the molecular gas, due to the difficulty in estimating atomic gas masses in galaxies at $z \gtrsim 0.25$, where it is very difficult to detect the weak H I 21 cm emission line. Molecular emission studies of star-forming galaxies have obtained typical gas depletion timescales of ≈ 0.5–1 Gyr (e.g., Saintonge et al. 2011; Tacconi et al. 2013; Genzel et al. 2015; Schinnerer et al. 2016) for main-sequence galaxies at $z \approx 0$–4. At high redshifts, the molecular gas depletion timescale shows only a weak dependence on redshift and stellar mass, but a strong dependence on the sSFR (Genzel et al. 2015). However, at low redshifts, this timescale has been found to depend on stellar mass: the molecular gas depletion timescale is larger by a factor of ≈ 6 in the highest-mass galaxies (Saintonge et al. 2011). We note that a recent study of molecular gas in absorption-selected galaxies at $z \approx 0.7$ has found evidence for significantly longer molecular gas depletion timescales, $\gtrsim 10$ Gyr (Kanekar et al. 2018), very different from those seen in emission-selected star-forming galaxies.

In the local universe, Saintonge et al. (2011) used the *COLD GASS* galaxy sample, comprising of galaxies at $0.025 < z < 0.05$ with stellar mass $M_\star \geqslant 10^{10}\,M_\odot$, to study the dependence of the atomic gas depletion time on galaxy properties. They found that the average atomic gas depletion timescale is ≈ 3 Gyr (albeit with considerable scatter) for the *COLD GASS* galaxies, with little dependence on parameters like the stellar mass, the sSFR, etc. (see also Schiminovich et al. 2010). The molecular and atomic gas depletion timescales are similar in the highest-mass *COLD GASS* galaxies, with red colors and high surface densities, while the molecular gas depletion timescale is nearly an order of magnitude lower than the atomic gas depletion timescale in low-mass galaxies, with high sSFRs and low stellar surface density (Saintonge et al. 2011). Similarly, extending to lower stellar masses, $M_\star \geqslant 10^9\,M_\odot$, the galaxies of the *xGASS* "representative sample" of Catinella et al. (2018) have a median atomic gas depletion time of ≈ 5 Gyr, for objects with detections of H I 21 cm emission.

In the case of the DEEP2 galaxies, Kanekar et al. (2016) stacked the H I 21 cm emission from 868 galaxies at $z \approx 1.3$ to obtain an upper limit of $M_{\rm H\,I}(3\sigma) \leqslant 2.1 \times 10^{10}\,M_\odot$ on their average H I mass. We have stacked the rest-frame 1.4 GHz radio continuum emission from the same 868 galaxies, to obtain an SFR of $(24.2 \pm 3.7)\,M_\odot\,{\rm yr}^{-1}$. Combining this with the upper limit of Kanekar et al. (2016) on the H I mass then implies a 3σ upper limit of ≈ 0.87 Gyr on the atomic gas depletion time, in main-sequence star-forming galaxies at $z \approx 1.3$. Interestingly enough, the atomic gas depletion timescale is comparable to the molecular gas depletion timescale (≈ 0.7 Gyr) in similar star-forming galaxies at a similar redshift (Tacconi et al. 2013; Genzel et al. 2015). The DEEP2 galaxies of the subsample of Kanekar et al. (2016) have stellar masses $\gtrsim 10^9\,M_\odot$, similar to those of the *xGASS* sample, but have far shorter atomic gas depletion times. The short inferred gas depletion time of the DEEP2 subsample emphasizes the need for replenishment of the atomic gas content of high-z main-sequence galaxies. Atomic hydrogen thus appears to be a transient phase in star-forming galaxies at high redshifts, with the conversion from the atomic to the molecular phase taking place on a timescale comparable to the timescale for the conversion of the molecular gas to stars. This is consistent with the speculation of Saintonge et al. (2011), that, at high redshifts, the bottleneck for star formation does not lie in the conversion of atomic gas to molecular gas.

Krumholz et al. (2008, 2009) carried out a theoretical modeling of the formation of molecular hydrogen from the atomic phase in galactic disks, considering the atomic to molecular transition to take place in a thin spherical layer, separating a purely molecular region from a region with a negligible molecular fraction (see also Krumholz 2013), and finding reasonable agreement with observational data on local samples of galaxies. We use this model to examine conditions in the DEEP2 galaxies that might yield the observed atomic and molecular gas depletion timescales of <0.87 Gyr and ≈ 0.7 Gyr, respectively. In chemical equilibrium, the atomic and molecular gas depletion timescales are related by

$$\Delta t_{\rm H\,I} = \Delta t_{\rm H_2} / R_{\rm H_2}, \qquad (8)$$

where $\Delta t_{\rm H\,I}$ and $\Delta t_{\rm H_2}$ are the atomic and molecular gas depletion timescales, and $R_{\rm H_2}$ is the atomic-to-molecular mass ratio, with

$$R_{\rm H_2} = f_{\rm H_2} / [1 - f_{\rm H_2}], \qquad (9)$$

and $f_{\rm H_2}$ is the H$_2$ fraction.

Equations (10)–(12) of Krumholz (2013) relate $f_{\rm H_2}$ to the total gas surface density Σ_0, the clumping factor $f_{\rm c}$, and the metallicity. Krumholz (2013) note that the gas clumping factor depends on the scale over which the surface density is averaged, with $f_{\rm c} \approx 1$ on scales of ≈ 100 pc, and $f_{\rm c} \approx 5$ on scales of ≈ 1 kpc. We will assume $f_{\rm c} \approx 5$ averaged over the DEEP2 galaxies. Finally, we assume that the DEEP2 galaxies have, on average, solar metallicity.

For the DEEP2 galaxies, the gas depletion timescales are $\Delta t_{\rm H\,I} < 0.87$ Gyr, and $\Delta t_{\rm H_2} \approx 0.7$ Gyr (Tacconi et al. 2013), implying $R_{\rm H_2} \geqslant 0.8$. Using this and $f_{\rm c} \approx 5$ in Equations (10–12) of Krumholz (2013) then yields an average total gas surface density of $\Sigma_0 \gtrsim 6\,M_\odot\,{\rm pc}^{-2}$. Overall, within the model of Krumholz (2013), the average gas surface density in the DEEP2 galaxies must be relatively high to account for the similar atomic and molecular gas depletion timescales.

5. Summary

We have carried out deep GMRT 610 MHz imaging of four subfields of the DEEP2 Galaxy Survey, achieving rms noise values of ≈ 14–$39\ \mu$Jy/Beam in the different fields. We have detected the stacked rest-frame 1.4 GHz radio continuum emission from a near-complete ($M_B \leqslant -21$) sample of 3698 blue star-forming galaxies at $0.7 \lesssim z \lesssim 1.45$, and use the stacked images to study the redshift evolution of the SFR, the sSFR, and the main sequence of star-forming galaxies. This is the first study of high-z star-forming galaxies where such radio stacking has been carried out at frequencies close to the rest-frame 1.4 GHz frequency, so that assumptions about the slope of synchrotron emission do not affect our results. We obtain a median total SFR of $(24.4 \pm 1.4)\ M_\odot\ \mathrm{yr}^{-1}$ for the 3698 galaxies of the sample. We also find that the stacked continuum emission is unresolved, with a transverse size <8 kpc at the median sample redshift of $z_{\mathrm{med}} \approx 1.1$. We find that both the median SFR and the median sSFR decrease with decreasing redshift, with SFR $\propto (1 + z)^{1.98 \pm 0.50}$ and sSFR $\propto (1 + z)^{3.94 \pm 0.57}$ over $0.7 \lesssim z \lesssim 1.45$, consistent with earlier studies based on other SFR indicators. We clearly detect the main-sequence relation between SFR and stellar mass, with SFR $= (13.4 \pm 1.8) \times [M_\star/(10^{10}\ M_\odot)]^{(0.73 \pm 0.09)}\ M_\odot\ \mathrm{yr}^{-1}$. We also find weak evidence that the normalization of the main sequence increases by a factor of ≈ 1.6 from $z \approx 0.85$ to ≈ 1.2; however, we find no evidence for changes in the main sequence slope over this redshift range. We compare the median SFRs estimated from other indicators, the [O II]$\lambda 3727$ line luminosity, the rest-frame NUV continuum luminosity, and the rest-frame U-band continuum luminosity, with the median total SFR inferred from our stacking analysis to infer the dust extinction correction factor for each tracer. We obtain dust extinction correction factors of ≈ 2.0, ≈ 4.7, and ≈ 2.5 for the above three tracers, respectively, with the largest correction factor for the NUV luminosity and the smallest for the [OII]$\lambda 3727$ line luminosity. This indicates that significant dust extinction is present in the DEEP2 galaxies. We find that the dust extinction correction factors do not appear to vary with redshift, over $0.7 \lesssim z \lesssim 1.45$, but increase with increasing color and stellar mass, for all SFR tracers. Nebular emission appears to suffer less extinction than the stellar continuum in the DEEP2 galaxies, contrary to the situation in galaxies in the local universe and a few studies of galaxies at high redshifts. However, the relative extinction increases with both increasing stellar mass and color, with redder, more-massive galaxies showing higher extinction in the nebular emission than in the stellar continuum. This suggests that the actively star-forming regions in red, massive galaxies at $z \approx 1$ already contain significant amounts of a second dust component, different from that in the extended galactic disk. We also find that the ratio of nebular extinction to stellar extinction in the DEEP2 galaxies increases with decreasing redshift; extrapolating this relation to $z = 0$, we find that this ratio is consistent with estimates of the excess extinction suffered by nebular emission relative to the stellar continuum in nearby star-forming galaxies. Finally, we combine our median radio SFR estimates with the upper limit on the average H I mass of a subsample of the DEEP2 galaxies at $z \approx 1.3$ to obtain an upper limit of 0.87 Gyr on the atomic gas depletion time for star-forming galaxies at this redshift. This is the first constraint on the atomic gas depletion time in star-forming galaxies at $z \gtrsim 1$; the low value of the gas depletion time suggests that H I is likely to be a transient phase in star-forming galaxies, with efficient conversion of atomic gas to molecular gas, on a timescale similar to that of the conversion of the molecular gas to stars.

ORCID iDs

Nissim Kanekar https://orcid.org/0000-0002-9757-7206
Benjamin J. Weiner https://orcid.org/0000-0001-6065-7483

References

Ade, P. A. R., Aghanim, N., Arnaud, M., et al. 2016, A&A, 594, A13
Battisti, A. J., Calzetti, D., & Chary, R.-R. 2016, ApJ, 818, 13
Battisti, A. J., Calzetti, D., & Chary, R.-R. 2017, ApJ, 851, 90
Bell, E. F. 2003, ApJ, 586, 794
Bouwens, R. J., Bradley, L., Zitrin, A., et al. 2014, ApJ, 795, 126
Brinchmann, J., Charlot, S., White, S. D. M., et al. 2004, MNRAS, 351, 1151
Calzetti, D. 1997, AJ, 113, 162
Calzetti, D., Armus, L., Bohlin, R. C., et al. 2000, ApJ, 533, 682
Calzetti, D., Kinney, A. L., & Storchi-Bergmann, T. 1994, ApJ, 429, 582
Cardelli, J. A., Clayton, G. C., & Mathis, J. S. 1989, ApJ, 345, 245
Carilli, C. L., Lee, N., Capak, P., et al. 2008, ApJ, 689, 883
Catinella, B., Saintonge, A., Janowiecki, S., et al. 2018, MNRAS, 476, 875
Charlot, S., & Fall, S. M. 2000, ApJ, 539, 718
Cid Fernandes, R., Mateus, A., Sodré, L., Stasińska, G., & Gomes, J. M. 2005, MNRAS, 358, 363
Condon, J. J. 1992, ARA&A, 30, 575
Condon, J. J., Cotton, W. D., & Broderick, J. J. 2002, AJ, 124, 675
Cornwell, T. J., Golap, K., & Bhatnagar, S. 2008, ISTSP, 2, 647
Cowie, L. L., Songaila, A., Hu, E. M., & Cohen, J. G. 1996, AJ, 112, 839
Cram, L., Hopkins, A., Mobasher, B., & Rowan-Robinson, M. 1998, ApJ, 507, 155
Daddi, E., Dickinson, M., Morrison, G., et al. 2007, ApJ, 670, 156
Dickinson, M., Giavalisco, M. & GOODS Team 2003, in The Mass of Galaxies at Low and High Redshift, ed. R. Bender & A. Renzini (Berlin: Springer), 324
Dunne, L., Ivison, R. J., Maddox, S., et al. 2009, MNRAS, 394, 3
Elbaz, D., Daddi, E., Le Borgne, D., et al. 2007, A&A, 468, 33
Erb, D. K., Shapley, A. E., Pettini, M., et al. 2006, ApJ, 644, 813
Fanelli, M. N., O'Connell, R. W., & Thuan, T. X. 1988, ApJ, 334, 665
Förster Schreiber, N. M., Genzel, R., Bouché, N., et al. 2009, ApJ, 706, 1364
Fumagalli, M., Hennawi, J. F., Prochaska, J. X., et al. 2014, ApJ, 780, 74
Genzel, R., Tacconi, L. J., Lutz, D., et al. 2015, ApJ, 800, 20
Giavalisco, M., Ferguson, H. C., Koekemoer, A. M., et al. 2004, ApJL, 600, L93
Gordon, K. D., Clayton, G. C., Misselt, K. A., Landolt, A. U., & Wolff, M. J. 2003, ApJ, 594, 279
Hao, C.-N., Kennicutt, R. C., Johnson, B. D., et al. 2011, ApJ, 741, 124
Hopkins, A. M., & Beacom, J. F. 2006, ApJ, 651, 142
Hopkins, A. M., Miller, C. J., Nichol, R. C., et al. 2003, ApJ, 599, 971
Ilbert, O., Arnouts, S., Le Floc'h, E., et al. 2015, A&A, 579, A2
Kanekar, N., Prochaska, J. X., Christensen, L., et al. 2018, ApJL, 856, L23
Kanekar, N., Sethi, S., & Dwarakanath, K. S. 2016, ApJL, 818, L28
Karim, A., Schinnerer, E., Martínez-Sansigre, A., et al. 2011, ApJ, 730, 61
Kashino, D., Silverman, J. D., Rodighiero, G., et al. 2013, ApJL, 777, L8
Kennicutt, R. C., & Evans, N. J. 2012, ARA&A, 50, 531
Kennicutt, R. C., Jr. 1998, ApJ, 498, 541
Kroupa, P., & Weidner, C. 2003, ApJ, 598, 1076
Krumholz, M. R. 2013, MNRAS, 436, 2747
Krumholz, M. R., McKee, C. F., & Tumlinson, J. 2008, ApJ, 689, 865
Krumholz, M. R., McKee, C. F., & Tumlinson, J. 2009, ApJ, 693, 216

Le Floc'h, E., Papovich, C., Dole, H., et al. 2005, ApJ, 632, 169
Madau, P., & Dickinson, M. 2014, ARA&A, 52, 415
Magnelli, B., Ivison, R. J., Lutz, D., et al. 2015, A&A, 573, A45
Mayya, Y. D., & Prabhu, T. P. 1996, AJ, 111, 1252
Murphy, E. J., Condon, J. J., Schinnerer, E., et al. 2011, ApJ, 737, 67
Newman, J. A., Cooper, M. C., Davis, M., et al. 2013, ApJS, 208, 5
Noeske, K. G., Weiner, B. J., Faber, S. M., et al. 2007, ApJ, 660, L43
Pannella, M., Carilli, C. L., Daddi, E., et al. 2009, ApJL, 698, L116
Pannella, M., Elbaz, D., Daddi, E., et al. 2015, ApJ, 807, 141
Peng, Y.-J., Lilly, S. J., Kovač, K., et al. 2010, ApJ, 721, 193
Price, S. H., Kriek, M., Brammer, G. B., et al. 2014, ApJ, 788, 86
Puglisi, A., Rodighiero, G., Franceschini, A., et al. 2016, A&A, 586, A83
Reddy, N. A., Erb, D. K., Pettini, M., Steidel, C. C., & Shapley, A. E. 2010, ApJ, 712, 1070
Renzini, A. 2009, MNRAS, 398, L58
Sadler, E. M., Jackson, C. A., Cannon, R. D., et al. 2002, MNRAS, 329, 227
Saintonge, A., Kauffmann, G., Wang, J., et al. 2011, MNRAS, 415, 61
Saintonge, A., Lutz, D., Genzel, R., et al. 2013, ApJ, 778, 2
Salim, S., Rich, R. M., Charlot, S., et al. 2007, ApJS, 173, 267
Santini, P., Fontana, A., Grazian, A., et al. 2009, A&A, 504, 751
Schiminovich, D., Catinella, B., Kauffmann, G., et al. 2010, MNRAS, 408, 919
Schinnerer, E., Groves, B., Sargent, M. T., et al. 2016, ApJ, 833, 112
Scoville, N., Aussel, H., Brusa, M., et al. 2007, ApJS, 172, 1
Sklias, P., Schaerer, D., Elbaz, D., et al. 2017, A&A, 605, A29
Smolčić, V., Schinnerer, E., Scodeggio, M., et al. 2008, ApJS, 177, 14
Sullivan, M., Mobasher, B., Chan, B., et al. 2001, ApJ, 558, 72
Tacconi, L. J., Neri, R., Genzel, R., et al. 2013, ApJ, 768, 74
Tasca, L. A. M., Le Fèvre, O., Hathi, N. P., et al. 2015, A&A, 581, A54
Taylor, A. R., & Jagannathan, P. 2016, MNRAS, 459, L36
Tremonti, C. A., Heckman, T. M., Kauffmann, G., et al. 2004, ApJ, 613, 898
Weiner, B. J., Coil, A. L., Prochaska, J. X., et al. 2009, ApJ, 692, 187
Weiner, B. J., Papovich, C., Bundy, K., et al. 2007, ApJL, 660, L39
Whitaker, K. E., Franx, M., Leja, J., et al. 2014, ApJ, 795, 104
White, R. L., Helfand, D. J., Becker, R. H., Glikman, E., & de Vries, W. 2007, ApJ, 654, 99
Wild, V., Charlot, S., Brinchmann, J., et al. 2011, MNRAS, 417, 1760
Willmer, C. N. A., Faber, S. M., Koo, D. C., et al. 2006, ApJ, 647, 853
Wuyts, S., Förster Schreiber, N. M., Nelson, E. J., et al. 2013, ApJ, 779, 135
Yun, M. S., Reddy, N. A., & Condon, J. J. 2001, ApJ, 554, 803